PAPER

Check for updates

Confined oriented growth of FeSe$_2$ on a porous graphene film as a binder-free anode for high-rate lithium-ion batteries†

Xiaoting Zhang, [ID] [a] Jiaxiu Diao,[a] Jinghao Qiao,[a] Yuhui Wen,[a] Hongkun Zhang [ID] *[bc] and Rui Wang*[a]

FeSe$_2$ nanorod@porous graphene films (FeSe$_2$@PG) were prepared by simple vacuum filtration, annealing, and subsequent selenylation. These FeSe$_2$ nanorods were formed *via* confined oriented growth of FeSe$_2$ nanoparticles. The morphology of FeSe$_2$@PG was characterized using scanning electron microscopy (SEM) and transmission electron microscopy (TEM). The interfacial interaction between FeSe$_2$ and graphene was investigated using X-ray photoelectron spectroscopy (XPS) and Raman spectroscopy. When used as an anode in lithium-ion batteries, the FeSe$_2$@PG electrode exhibited an initial reversible capacity of 858 mA h g^{-1}, which was increased to 1053 mA h g^{-1} after 50 cycles at 100 mA g^{-1}. At high rates of 1, 2, 5, and 10 A g^{-1}, the electrode maintained specific capacities of 483, 313, 265, and 178 mA h g^{-1}, respectively, even after 1000 cycles. The excellent electrochemical performance of the FeSe$_2$@PG electrode is attributed to the special structure of FeSe$_2$@PG and the strong covalent bonds between graphene and FeSe$_2$. Moreover, graphene can not only act as a substrate for the growth of FeSe$_2$ nanorods, but also improve the conductivity of FeSe$_2$. Furthermore, the porous structure of graphene can reduce the diffusion path of lithium ions and improve the penetration of the electrolyte into the graphene layer. In addition, a new covalent bond of C–Se–Fe was formed between graphene and FeSe$_2$, which was beneficial for maintaining its structural stability.

Introduction

Energy crisis and environmental degradation have become two major problems in the world.[1] Thus, the goal of carbon neutrality has been proposed. The development of clean renewable energy is one of the effective strategies for solving the above problems. Rechargeable lithium-ion batteries (LIBs) have become an important means for energy storage owing to their high capacity, high energy density, high operating voltage, and suitable working temperature.[2–4] However, graphite, a mainstream commercial anode material, can hardly meet the increasing requirements of

various energy storage devices such as electric vehicles and consumer electronics because of its low theoretical specific capacity (372 mA h g^{-1}).[5] Transition-metal chalcogenides are considered outstanding anode candidates owing to their high theoretical specific capacity, low cost, and environmental friendliness.[6–8] Compared with transition-metal oxides and sulfides, metal selenides (MSe) exhibit superior electrical conductivity and higher stack density.[9,10] Among them, FeSe$_2$ is considered a promising anode material for LIBs owing to its high theoretical capacity, low toxicity, and good chemical stability.[11,12] However, similar to other chalcogenide compounds, MSe also face the issue of serious volume expansion during charging and discharging. Pulverization of electrode materials may occur and even separate from the current collector, resulting in rapid capacity attenuation and deterioration of cycle performance.[13] Moreover, although the conductivity of FeSe$_2$ is better than those of metal oxides and sulfides, it still does not meet the requirements for application in LIBs. To improve its electrochemical performance, a commonly used method is the preparation of nanocarbon-based selenide metal composites.[14]

Graphene, a two-dimensional carbon nanomaterial, has been considered an ideal material owing to its superior electronic conductivity and chemical stability.[15,16] However, because

[a] *Beijing Key Laboratory of Clothing Materials R & D and Assessment, Beijing Engineering Research Center of Textile Nanofiber, School of Materials Design & Engineering, Beijing Institute of Fashion Technology, Beijing 100029, China. E-mail: clywangrui@bift.edu.cn*

[b] *GRINM Group Corporation Limited, Beijing 100088, China. E-mail: zhk@cutc.net*

[c] *China United Test & Certification Co., Ltd, Beijing 101407, China*

† Electronic supplementary information (ESI) available: The TG curves of FeSe$_2$@PG-4, FeSe$_2$@PG-6, and FeSe$_2$@PG. The SEM images of FeSe$_2$@PG-4, FeSe$_2$@PG-6, and FeSe$_2$@PG electrodes after cycling. The area and area ratio of different covalent bonds in the C 1s and Se 3d spectra of FeSe$_2$@PG-4, FeSe$_2$@PG-6, and FeSe$_2$@PG. The AC impedance resistances of FeSe$_2$@PG-4, FeSe$_2$@PG-6, and FeSe$_2$@PG. See DOI: https://doi.org/10.1039/d3ma00269a

of the planar structure of graphene, the ionic steric effect blocks the fast transmission of lithium ions in high-power batteries, thereby affecting the electrochemical properties of graphene-based electrode materials.[17] Porous graphene not only improves the conductivity of $FeSe_2$, but also avoids the blockage of the lithium-ion transmission path caused by the ionic steric effect due to its special porous structure. This is beneficial for decreasing the polarization, reducing the diffusion distance of lithium ions, and promoting the infiltration of the electrolyte on MSe, thus improving the electrochemical performance.[18,19] For example, Rui *et al.* synthesized rod-like $FeSe_2$-C wrapped with reduced graphene, which exhibited excellent performance as an anode material for LIBs.[20] Qian *et al.* reported $FeSe_2$/carbon matrix nanoparticles embedded into N-doped graphene sheets, which exhibited superior Li storage performance.[21] Xiong *et al.* prepared $FeSe_2$@reduced graphene oxide composites *via* a facile one-step hydrothermal technique, which showed superior specific capacity and good cycling stability.[22] However, the majority of reported materials are in a powder form, and electrodes are often prepared through the slurry-coating method in a current collector using conducting additives and insulating binders. These additives and binders increase the cost and decrease the energy density of batteries without any capacity contribution.[23,24] Thus, designing free-standing anode materials without conducting agents and binders is considerably important. In addition, the interfacial binding mechanism of $FeSe_2$ with graphene must be elucidated.

Herein, we report the confined oriented growth of $FeSe_2$ nanorods from nanoparticles on a porous graphene film *via* vacuum filtration, annealing, and subsequent selenylation to prepare a free-standing anode material without binders. Moreover, graphene is used as a highly conductive substrate to effectively connect with $FeSe_2$. Furthermore, its porous structure provides abundant open channels for lithium-ion transport, shortens the diffusion distance of lithium ions, and increases the infiltration of the electrolyte. The $FeSe_2$ nanorods are embedded in the pores of graphene films and selenium bridges are formed between $FeSe_2$ and porous graphene. $FeSe_2$@PG exhibits high specific capacity, superior rate performance, and stable cyclability when used as an anode material for LIBs. The excellent electrochemical performance of the electrode material is attributed to the highly conductive network formed by the graphene film and the tight covalent bonds between $FeSe_2$ and graphene.

Experimental

Synthesis of $FeSe_2$@PG

$FeSe_2$@PG was prepared *via* facile vacuum filtration, annealing, and subsequent selenylation. Fe_3C@PG was synthesized by mixing ferric nitrate and graphene oxide (fabricated using a modified Hummers' method using natural graphite[25]), filtration and followed by annealing at 1000 °C for 1 h in an argon gas atmosphere, as described in our previous work.[26] Finally, the Fe_3C@PG film and Se powders (0.6 g) were loaded into a quartz boat and placed in a tube furnace. $FeSe_2$@PG was obtained after annealing at 400 °C for 8 h in a H_2 (15%)/Ar

(85%) atmosphere. To investigate the formation process of $FeSe_2$@PG, selenization was performed for 4 and 6 h; the obtained samples were labeled as $FeSe_2$@PG-4 and $FeSe_2$@PG-6, respectively.

Characterization

The morphology and structure of the obtained samples were investigated using scanning electron microscopy (SEM, JEOL JSM-7500F), transmission electron microscopy (TEM, JEOL JEM-2100F), and X-ray diffraction (XRD, Rigaku D/max-2500B2+/PCX) using Cu Kα radiation (λ = 1.5406 Å) over the range of 5–90° (2θ) at room temperature. X-ray photoelectron energy spectra (XPS) were recorded using monochromatized Al Kα radiation (1486.6 eV) with a 30 eV pass energy in 0.5 eV step over an area of 0.65 mm × 0.65 mm. The Raman spectra (WITec alpha 300) were investigated from 1000 to 2000 cm^{-1} at room temperature with an excitation line of 532 nm. The contents of $FeSe_2$ in $FeSe_2$@PG were investigated using thermogravimetry (TG) measurements. The samples were heated from room temperature to 700 °C at 5 °C min^{-1} under an O_2 atmosphere.

Electrochemical measurements

Lithium-ion storage performance was characterized using 2032 coin-type cells. The $FeSe_2$@PG films were directly used as the working electrodes without any conductive additives and binders. A pure lithium sheet was used as the counter electrode, polypropylene served as the separator, and a solution of 1 M $LiPF_6$ in ethylene carbonate (EC)–diethyl carbonate (DEC) (1 : 1 by volume) was used as the electrolyte. The electrochemical performance was tested in a voltage window of 0.01–3.0 V using a Land battery test system (CT3001A, WUHAN LAND). Electrochemical impedance spectroscopy (EIS) was performed on a CHI600E electrochemical working station (Shanghai Chenhua). The frequency range for the EIS measurements was from 10^5 Hz to 10^{-2} Hz.

Results and discussion

Fig. 1 illustrates the preparation process of $FeSe_2$@PG-4, $FeSe_2$@PG-6, and $FeSe_2$@PG. First, the Fe_3C@PG film was
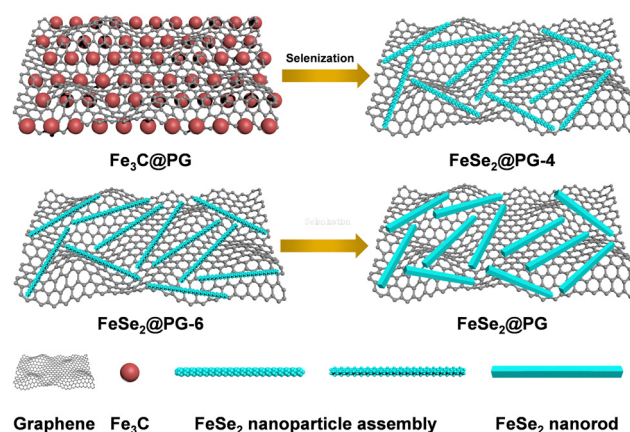

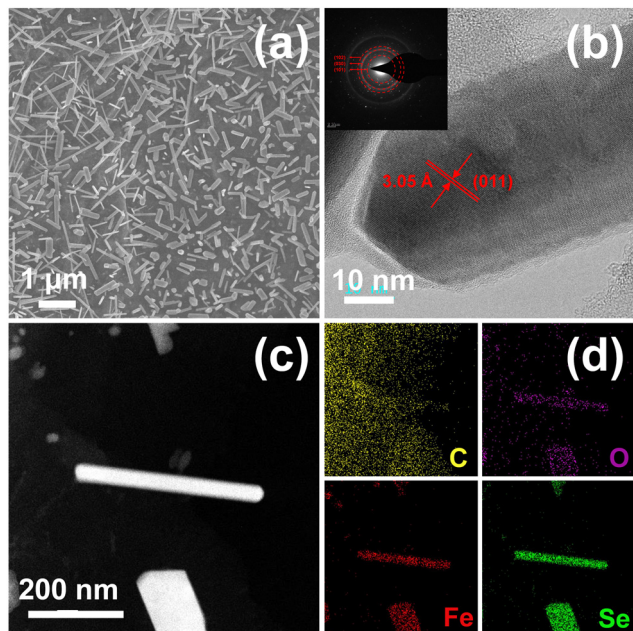Fig. 1 Schematic diagram of the formation process of $FeSe_2$@PG.

Fig. 2 (a) SEM, (b) HRTEM, and (c) STEM images of FeSe$_2$@PG and (d) corresponding elemental mapping of C, O, Fe, and Se (the insets show the corresponding SAED pattern).

Fig. 3 SEM images of (a) Fe$_3$C@PG, (b) FeSe$_2$@PG-4, (c) FeSe$_2$@PG-6, and (d) FeSe$_2$@PG.

prepared *via* vacuum filtration and carbonization using graphene oxide and ferric nitrate as raw materials. Subsequently, the Fe$_3$C@PG film was converted to FeSe$_2$@PG-4, FeSe$_2$@PG-6, and FeSe$_2$@PG *via* selenization using Se powder at 400 °C for 4, 6, and 8 h, respectively. Fig. 2a shows FeSe$_2$ nanorods uniformly anchored on the surface of the graphene film. The crystalline lattice of FeSe$_2$ nanorods can be clearly observed in Fig. 2b, which is *ca.* 3.05 Å and corresponds to the (011) lattice plane of FeSe$_2$. The selected area electron diffraction (SAED) image of FeSe$_2$@PG shows diffraction spots matching (101), (030), and (101) diffraction rings, revealing that FeSe$_2$ nanorods are polycrystalline. The EDS mapping shows that the nanorods contain Fe and Se elements, which are uniformly distributed throughout the nanorod (Fig. 2c and d).

To figure out the formation process of FeSe$_2$ nanorods, samples obtained at various selenization times are investigated. The morphology of FeSe$_2$ varies considerably with increasing selenization times. Fig. 3a shows iron carbide nanoparticles located exactly in the pores of porous graphene. Ferric carbide is derived from the reaction between graphene and iron oxide, which originates from the pyrolysis of ferric nitrate. The formation of pores can be attributed to the carbothermal reaction between graphene and ferric nitrate.[27–29] When the Fe$_3$C@PG film is selenized at 400 °C for 4 h, an iron diselenide assembly composed of fine FeSe$_2$ nanoparticles with a diameter of ∼30 nm is formed (Fig. 3b). With the increase of selenization time, iron diselenide nanoparticles continuously grow and a certain degree of fusion occurs. When the selenization time is 6 h, the FeSe$_2$ nanorods with a small number of nanoparticles on the surface are formed (Fig. 3c). Finally, when the selenization time is 8 h, the FeSe$_2$ nanorods with a smooth surface are
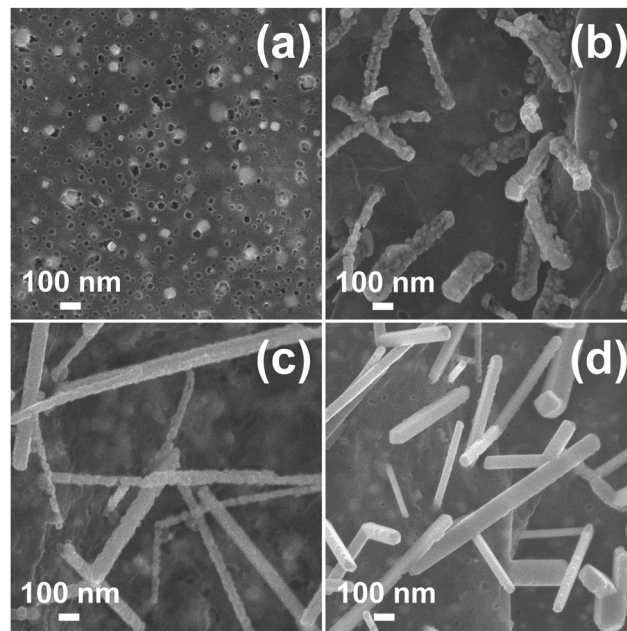
obtained (Fig. 3d). According to the TG results, the contents of FeSe$_2$ in FeSe$_2$@PG-4, FeSe$_2$@PG-6, and FeSe$_2$@PG are 11.82%, 13.46%, and 17.23%, respectively (Fig. S1, ESI†). Fig. 4 depicts the typical XRD patterns of FeSe$_2$@PG-4, FeSe$_2$@PG-6, and FeSe$_2$@PG. All the peaks match well with those of FeSe$_2$ (JCPDS 21-0432). However, the intensities of the diffraction peaks of FeSe$_2$ increase with the selenization time, indicating the progressive crystallization of iron diselenide. Therefore, it is reasonable to infer that the formation process of iron diselenide nanorods can be attributed to the oriented attachment (OA) mechanism.[30–32] First, FeSe$_2$ nanoparticles are formed on the surface of graphene. Second, FeSe$_2$ nanoparticles move along graphene and connect with each other to form a corn-like FeSe$_2$ assembly. Furthermore, FeSe$_2$ nanoparticles continuously fuse to form nanorods with a few particles on the surface. Finally, FeSe$_2$ nanorods with a smooth surface are formed with a further fusion of FeSe$_2$ nanoparticles *via* atom-to-atom reorientations by the migration of grain boundaries or dislocations.[32–34]

Along with the formation of FeSe$_2$ nanorods, some chemical connections between FeSe$_2$ and graphene are formed, which is confirmed *via* XPS. FeSe$_2$@PG-4, FeSe$_2$@PG-6, and FeSe$_2$@PG are all composed of C, O, Fe, and Se elements (Fig. 5a). The C 1s and Se 3d curves are fitted using the Gaussian–Lorentzian peak shape after a Shirley background correction. The C 1s spectra of three samples are fitted to the C (C=C/C–C) in aromatic rings (285 eV), the C in C–O (286.7 eV), the C in C–Se (285.5 eV), and the C in C=O (288.6 eV) bonds (Fig. 5b).[35–37] With the extension of selenization time, the C–Se content increases from 15.0% (FeSe$_2$@PG-4) to 25.1% (FeSe$_2$@PG), indicating a stronger connection between graphene and FeSe$_2$ in FeSe$_2$@PG than in FeSe$_2$@PG-4 and FeSe$_2$@PG-6 (Tables S1 and S3, ESI†). To further analyze the interfacial interaction between graphene and FeSe$_2$, the Se 3d
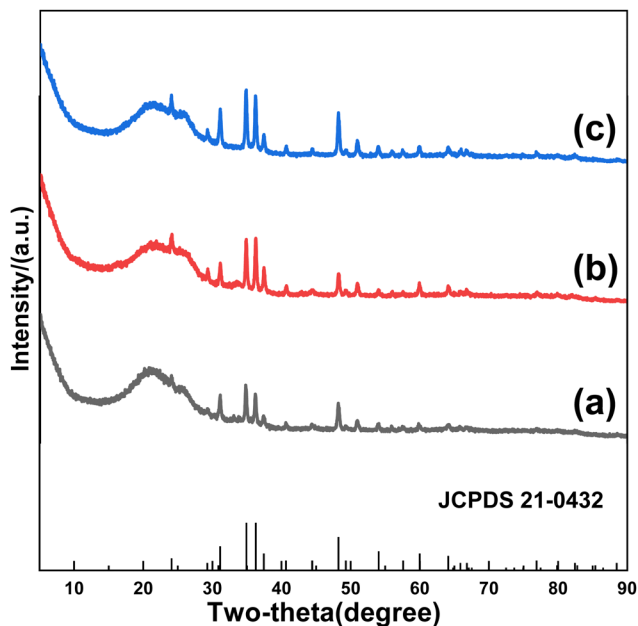
Fig. 4 XRD patterns of (a) FeSe$_2$@PG-4, (b) FeSe$_2$@PG-6, and (c) FeSe$_2$@PG.

spectra are investigated in detail (Fig. 5c). The spectra of three samples are fitted by six components at *ca.* 59.3, 57.9, 57.3, 56.5, 55.8, and 55.2 eV. The peak at 56.5 eV is attributed to Se–Se and that at 59.3 eV is attributed to Se–O.[38,39] The peaks at 55.2 and 55.8 eV are attributed to the covalent bond between selenium and iron.[40,41] In addition, the weak peak at around 57.9 eV is ascribed to C–Se–C. The middle peak at 57.3 eV corresponds to the interfacial interaction between FeSe$_2$ and graphene,[42] indicating the formation of C–Se–Fe bonds between the graphene and FeSe$_2$. It is worth noting that the content of the C–Se–Fe covalent bond in FeSe$_2$@PG is higher by 5.0% than that in FeSe$_2$@PG-4 (Tables S2 and S4, ESI†). This implies that the interfacial interaction between FeSe$_2$ and graphene is stronger in FeSe$_2$@PG.

In order to further investigate the interfacial properties, Raman measurements were performed. Raman spectroscopy was used to characterize not only the defects of carbon nanomaterials but also the interfacial interaction between carbonaceous materials and metal-containing compounds.[43] Fig. 6 depicts a typical D (*ca.* 1348 cm^{-1}) and G (*ca.* 1586 cm^{-1}) bands for carbon, and the intensity ratio of the D to the G bands (I_D/I_G) is used to measure the defects of carbon materials. The I_D/I_G ratios of FeSe$_2$@PG-4, FeSe$_2$@PG-6, and FeSe$_2$@PG are 1.28, 1.19, and 1.12, respectively. The lower I_D/I_G ratio of FeSe$_2$@PG implies a stronger interfacial interaction between graphene and FeSe$_2$, which is consistent with the XPS results.[43]

To investigate the effect of the interfacial interaction between graphene and FeSe$_2$ on the electrochemical performance of FeSe$_2$@porous graphene electrodes, the specific capacity, cycling and rate performance, and dynamic parameters of FeSe$_2$@PG-4, FeSe$_2$@PG-6, and FeSe$_2$@PG as anode materials for LIBs were evaluated *via* galvanostatic charge/discharge measurements. Fig. 7a–c show the initial three discharge–charge curves of

FeSe$_2$@PG-4, FeSe$_2$@PG-6, and FeSe$_2$@PG at 100 mA g^{-1}. It is worth noting that the initial coulombic efficiency is not high, as shown in Fig. 7a–c. The low initial coulombic efficiency can be attributed to the large irreversible capacity due to the formation of solid electrolyte interphase (SEI) films. Moreover, the defects and edges of porous graphene also decreases the initial coulombic efficiency of FeSe$_2$@PG. To improve the coulombic efficiency, we can consider the following strategies. First, we can control the formation of SEI films or synthesize artificial SEI films. Second, defects of porous graphene can be controlled to reduce the initial irreversible capacity of FeSe$_2$@PG. Finally, the initial coulombic efficiency can be improved by optimizing the electrolyte and the binder. The plateaus at 2.0, 1.5, and 1.0 V during discharge are attributed to the lithiation of FeSe$_2$ to Li$_x$FeSe$_2$ (FeSe$_2$ + xLi$^+$ + xe$^-$ → Li$_x$FeSe$_2$), the conversion reaction of Li$_x$FeSe$_2$ to Li$_2$Se [Li$_x$FeSe$_2$ + (2−x)Li$^+$ + (2−x)e$^-$ → FeSe + Li$_2$Se], and the further transformation of FeSe to Fe and Li$_2$Se (FeSe + 2Li$^+$ + 2e$^-$ → Fe + Li$_2$Se), respectively.[44–46] The slope below 0.5 V is due to lithium intercalation into the graphene layers.[47] During the subsequent charging process, two plateaus are observed at 1.9 and 2.2 V, corresponding to Li$^+$ extraction processes [Fe + 2Li$_2$Se → Li$_x$FeSe$_2$ + (4−x)Li$^+$ + (4−x)e$^-$ and Li$_x$FeSe$_2$ → FeSe$_2$ + xLi$^+$ + xe$^-$].[48] The reversible capacities of FeSe$_2$@PG-4 and FeSe$_2$@PG-6 are 662 and 829 mA h g^{-1} at 100 mA g^{-1}, respectively. However, the specific capacity of FeSe$_2$@PG increases to 858 mA h g^{-1} at the same current density. After 50 cycles, FeSe$_2$@PG retains the reversible capacity of 1053 mA h g^{-1}, whereas that of FeSe$_2$@PG-4 is lower than 770 mA h g^{-1} at the same current density (Fig. 7d). Fig. 7e shows the rate capabilities of FeSe$_2$@PG-4, FeSe$_2$@PG-6, and FeSe$_2$@PG at different current densities between 0.1 and 10 A g^{-1}. The specific capacities of FeSe$_2$@PG at 1, 2, 5, and 10 A g^{-1} are 774, 664, 458, and 328 mA h g^{-1}, respectively. When the current density returns to 100 mA g^{-1}, the capacity immediately returns to 1046 mA h g^{-1} and then increases to 1187 mA h g^{-1} after 80 cycles, indicating the excellent rate performance of the FeSe$_2$@PG electrode (Fig. 7e). Fig. 7g shows that FeSe$_2$@PG exhibits stable cycling performance even at high current densities. At 1 A g^{-1}, the initial reversible capacity of FeSe$_2$@PG is 606 mA h g^{-1}. Notably, the specific capacity of FeSe$_2$@PG gradually decreases in the initial 100 cycles, which can be attributed to the poor electrolyte wetting of the FeSe$_2$@PG film. Subsequently, the specific capacity slowly increases and does not decay until 1000 cycles, which is due to the gradual electrolyte wetting.[49] After 1000 cycles, the specific capacity remains at 483 mA h g^{-1}. Even at higher current densities of 2, 5, and 10 A g^{-1}, FeSe$_2$@PG can still retain 313, 265, and 178 mA h g^{-1} after 1000 cycles, respectively. To analyze the better electrochemical performance of the FeSe$_2$@PG electrode, the microstructural changes in FeSe$_2$@PG-4, FeSe$_2$@PG-6, and FeSe$_2$@PG after the cycling test were determined and compared. Fig. S2 (ESI†) shows that FeSe$_2$ in FeSe$_2$@PG-4 and FeSe$_2$@PG-6 changed into small nanoparticles without any regulation. However, in the FeSe$_2$@PG electrode, FeSe$_2$ retains the rod-like structure integrity even though small nanoparticles are formed during cycling, indicating that the FeSe$_2$@PG electrode can resist the repeated intercalation and deintercalation of lithium ions
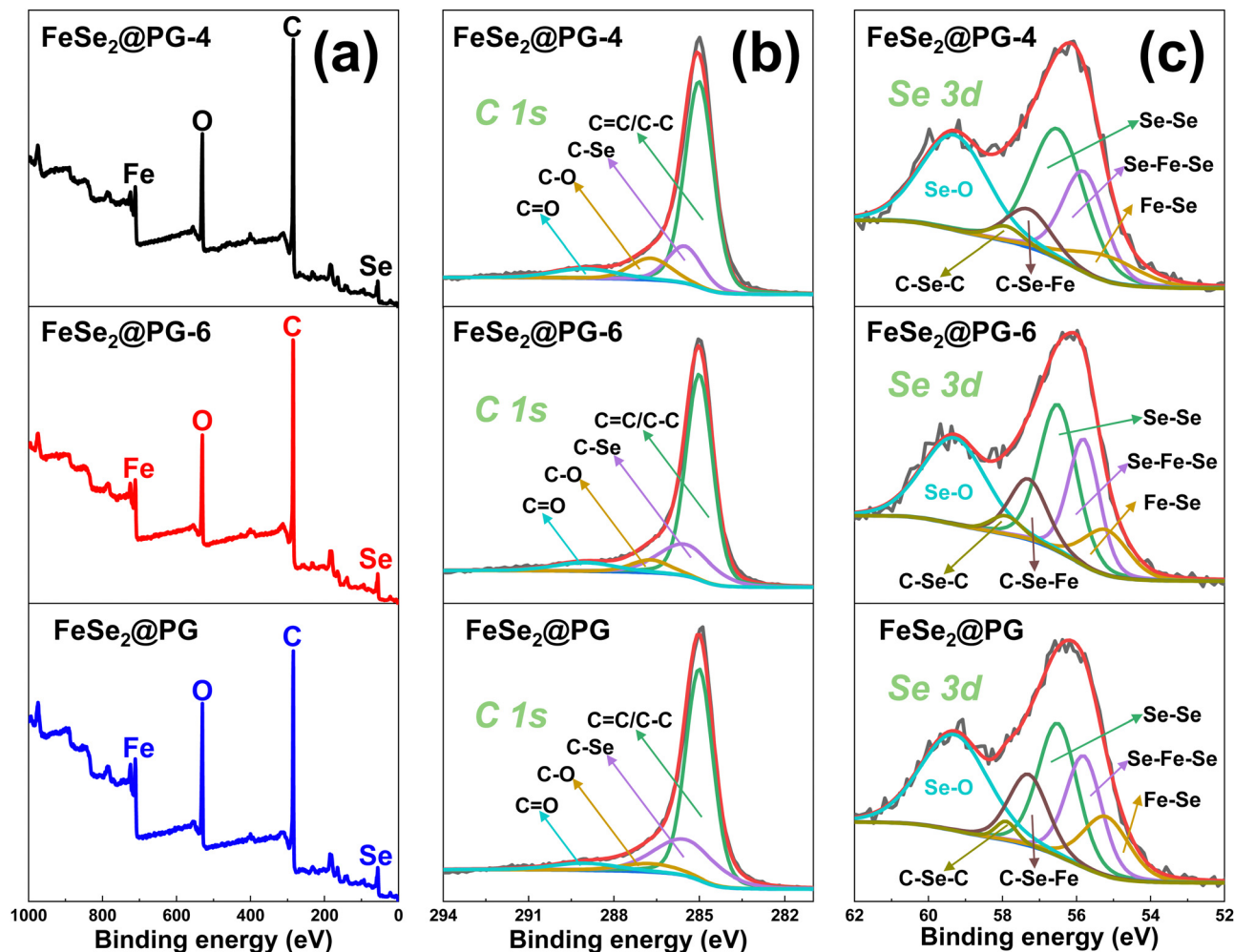
Fig. 5 (a) XPS spectra of FeSe$_2$@PG-4, FeSe$_2$@PG-6, and FeSe$_2$@PG and their (b) C 1s and (c) Se 3d spectra.
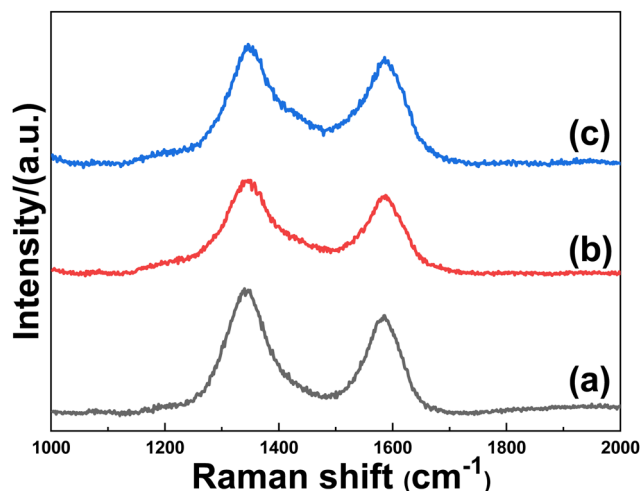

Fig. 6 Raman spectra of (a) FeSe$_2$@PG-4, (b) FeSe$_2$@PG-6, and (c) FeSe$_2$@PG.

during the charge/discharge process. It should be attributed to the stronger interfacial interaction between FeSe$_2$ and graphene in FeSe$_2$@PG than that in FeSe$_2$@PG-4 and FeSe$_2$@PG-6.

To elucidate the reasons for the differences in electrochemical performance, FeSe$_2$@PG-4, FeSe$_2$@PG-6, and FeSe$_2$@PG electrodes are investigated using EIS (Fig. 7f). The charge-transfer resistance and film resistance of FeSe$_2$@PG are lower than those of FeSe$_2$@PG-4 and FeSe$_2$@PG-6, which should be attributed to the strong interfacial interaction between FeSe$_2$ and graphene in FeSe$_2$@PG (Table S5, ESI†). In general, the excellent electrochemical performance of FeSe$_2$@PG can be ascribed to the following reasons. First, graphene can form a complete conductive network, which helps in improving the charge transfer reaction at high rates. Second, the porous structure of graphene provides fast transport channels for lithium ions and electrons. Finally, C–Se–Fe covalent bonds formed between graphene and FeSe$_2$ facilitate lithium ion diffusion and electron transfer. Therefore, the FeSe$_2$@PG electrode exhibits excellent electrochemical performance, including high specific capacity, good rate capability, and outstanding cycling stability, when used as an anode in LIBs.

Conclusions

FeSe$_2$@PG was prepared via the confined oriented growth of FeSe$_2$ on a porous graphene film. Graphene acted as a substrate

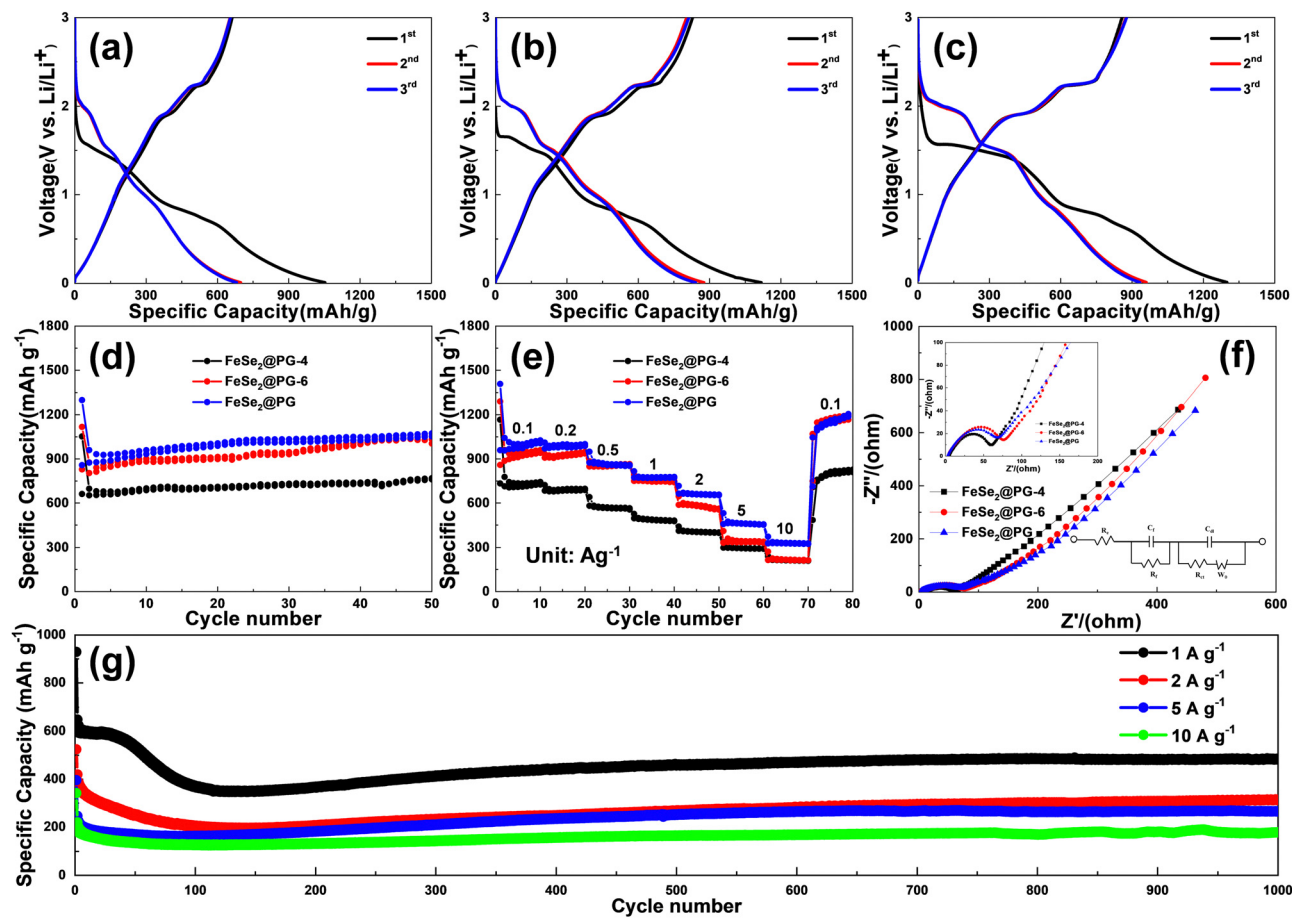**Fig. 7** Initial three discharge–charge curves of (a) FeSe$_2$@PG-4, (b) FeSe$_2$@PG-6, and (c) FeSe$_2$@PG at 100 mA g^{-1}. (d) Cycle performances of FeSe$_2$@PG-4, FeSe$_2$@PG-6, and FeSe$_2$@PG at 100 mA g^{-1}. (e) Rate capabilities of FeSe$_2$@PG-4, FeSe$_2$@PG-6, and FeSe$_2$@PG. (f) AC impedance spectra of FeSe$_2$@PG-4, FeSe$_2$@PG-6, and FeSe$_2$@PG and the corresponding Randles equivalent circuit. (g) Cycle performance of FeSe$_2$@PG at 1, 2, 5, and 10 A g^{-1}.

for the growth of FeSe$_2$ nanorods and improved the conductivity of the overall electrode material. In addition, C–Se–Fe covalent bonds were formed at the interface between FeSe$_2$ and graphene. The electrochemical performance of FeSe$_2$@PG was positively correlated with the content of C–Se–Fe covalent bonds. When used as an anode material for lithium ion batteries, FeSe$_2$@PG exhibited high capacity and excellent rate and cycle performance.

Conflicts of interest

There are no conflicts to declare.

Acknowledgements

Notes and references

1 F. Shaikh, Q. Ji and Y. Fan, *Renewable Sustainable Energy Rev.*, 2015, **52**, 1172–1185.

2 B. Dunn, H. Kamath and J.-M. Tarascon, *Science*, 2011, **334**, 928–935.

3 Y. Tang, Y. Zhang, W. Li, B. Ma and X. Chen, *Chem. Soc. Rev.*, 2015, **44**, 5926–5940.

4 L. Ji, Z. Lin, M. Alcoutlabi and X. Zhang, *Energy Environ. Sci.*, 2011, **4**, 2682–2699.

5 Y. Zhong, X. Xia, F. Shi, J. Zhan, J. Tu and H. J. Fan, *Adv. Sci.*, 2016, **3**, 1500286.

6 X. Zhang, J. Zhou, H. Song, X. Chen, Y. V. Fedoseeva, A. V. Okotrub and L. G. Bulusheva, *ACS Appl. Mater. Interfaces*, 2014, **6**, 17236–17244.

7 J. Ning, D. Zhang, H. Song, X. Chen and J. Zhou, *J. Mater. Chem. A*, 2016, **4**, 12098–12105.

8 H. Wu, S. Lu, S. Xu, J. Zhao, Y. Wang, C. Huang, A. Abdelkader, W. A. Wang, K. Xi, Y. Guo, S. Ding, G. Gao and R. V. Kumar, *ACS Nano*, 2021, **15**, 2506–2519.

9 X. Li, H. Wu, C. Guan, A. M. Elshahawy, Y. Dong, S. J. Pennycook and J. Wang, *Small*, 2019, **15**, 1803895.

10 C. Xia, Q. Jiang, C. Zhao, P. M. Beaujuge and H. N. Alshareef, *Nano Energy*, 2016, **24**, 78–86.

11 W. Xin, N. Chen, Z. Wei, C. Wang, G. Chen and F. Du, *Chem. – Eur. J.*, 2021, **27**, 3745–3752.

12 B. Cong, S. Sun, B. Wang, C. Lv, J. Zhao, F. Jin, J. Jia and G. Chen, *Chem. Eng. J.*, 2022, **435**, 135185.

13 Z. Liang, M. Yang, S. Wang, B. Chang, H. Tu, Y. Shao, B. Zhang, H. Zhao, Y. Lei and J. Shen, *Chem. Eng. J.*, 2021, **405**, 126724.

14 Q. Ma, L. Zhang, Y. Ding, X. Shi, Y. L. Ding, J. Mujtaba, Z. Li and Z. Fang, *J. Colloid Interface Sci.*, 2022, **622**, 840–848.

15 F. Bonaccorso, L. Colombo, G. Yu, M. Stoller, V. Tozzini, A. C. Ferrari, R. S. Ruoff and V. Pellegrini, *Science*, 2015, **347**, 1246501.

16 Y. Shao, M. F. El-Kady, L. J. Wang, Q. Zhang, Y. Li, H. Wang, M. F. Mousavi and R. B. Kaner, *Chem. Soc. Rev.*, 2015, **44**, 3639–3665.

17 F.-Y. Su, Y.-B. He, B. Li, X.-C. Chen, C.-H. You, W. Wei, W. Lv, Q.-H. Yang and F. Kang, *Nano Energy*, 2012, **1**, 429–439.

18 Y. Yang, Q. Lin, B. Ding, J. Wang, V. Malgras, J. Jiang, Z. Li, S. Chen, H. Dou, S. M. Alshehri, T. Ahamad, J. Na, X. Zhang and Y. Yamauchi, *Carbon*, 2020, **167**, 627–633.

19 J.-Q. Huang, X.-F. Liu, Q. Zhang, C.-M. Chen, M.-Q. Zhao, S.-M. Zhang, W. Zhu, W.-Z. Qian and F. Wei, *Nano Energy*, 2013, **2**, 314–321.

20 W. Ye, K. Wang, W. Yin, W. Chai, B. Tang and Y. Rui, *Electrochim. Acta*, 2019, **323**, 134817.

21 P. Jing, Q. Wang, B. Wang, X. Gao, Y. Zhang and H. Wu, *Carbon*, 2020, **159**, 366–377.

22 Z. Zhao, X. Teng, Q. Xiong, H. Chi, Y. Yuan, H. Qin and Z. Ji, *Sustainable Mater. Technol.*, 2021, **29**, e00313.

23 Z. Niu, P. Luan, Q. Shao, H. Dong, J. Li, J. Chen, D. Zhao, L. Cai, W. Zhou and X. Chen, *Energy Environ. Sci.*, 2012, **5**, 8726–8733.

24 T. Jin, Q. Han and L. Jiao, *Adv. Mater.*, 2020, **32**, 1806304.

25 W. S. Hummers Jr and R. E. Offeman, *J. Am. Chem. Soc.*, 1958, **80**, 1339.

26 X. Zhang, J. Zhou, X. Chen and H. Song, *ACS Appl. Energy Mater.*, 2018, **1**, 48–55.

27 D. Zhou, Y. Cui, P.-W. Xiao, M.-Y. Jiang and B.-H. Han, *Nat. Commun.*, 2014, **5**, 4716.

28 H. Cao, X. Zhou, C. Zheng and Z. Liu, *Carbon*, 2015, **89**, 41–46.

29 X. Zhang, J. Zhou, C. Liu, X. Chen and H. Song, *J. Mater. Chem. A*, 2016, **4**, 8837–8843.

30 R. L. Penn and J. F. Banfield, *Science*, 1998, **281**, 969–971.

31 G. Zhang, K. Liu, S. Liu, H. Song and J. Zhou, *J. Alloys Compd.*, 2018, **731**, 714–722.

32 D. Li, J. Zhou, X. Chen and H. Song, *ACS Appl. Mater. Interfaces*, 2018, **10**, 22841–22850.

33 X. Zhang, J. Zhang, J. Zhao, B. Pan, M. Kong, J. Chen and Y. Xie, *J. Am. Chem. Soc.*, 2012, **134**, 11908–11911.

34 L. Zhu, B. J. Richardson and Q. Yu, *Chem. Mater.*, 2015, **27**, 3516–3525.

35 Y. Li, Y. Xu, Z. Wang, Y. Bai, K. Zhang, R. Dong, Y. Gao, Q. Ni, F. Wu, Y. Liu and C. Wu, *Adv. Energy Mater.*, 2018, **8**, 1800927.

36 M. Ren, H. Zang, S. Cao, H. Guo, J. Zhang, W. Liu, J.-S. Yao, X. Zhang and Z. Zhou, *J. Mater. Chem. A*, 2023, **11**, 10435–10444.

37 X. Zhang, J. Zhou, H. Song, C. Liu, S. Zhang and X. Chen, *Carbon*, 2016, **99**, 370–374.

38 R. Manikandan, C. Justin Raj, G. Nagaraju, R. Velayutham, S. E. Moulton, J. Puigdollers and B. Chul Kim, *Chem. Eng. J.*, 2021, **414**, 128924.

39 J. Feng, S.-H. Luo, S.-X. Yan, Y. Zhan, Q. Wang, Y.-H. Zhang, X. Liu and L.-J. Chang, *J. Mater. Chem. A*, 2021, **9**, 1610–1622.

40 P. Ge, H. Hou, S. Li, L. Yang and X. Ji, *Adv. Funct. Mater.*, 2018, **28**, 1801765.

41 S. Jiang, M. Xiang, J. Zhang, S. Chu, A. Marcelli, W. Chu, D. Wu, B. Qian, S. Tao and L. Song, *Nanoscale*, 2020, **12**, 22210–22216.

42 F. Jin, M. Li, L. Xie and J. Jiang, *J. Power Sources*, 2021, **514**, 230587.

43 X. Zhang, C. Liu and R. Wang, *Sustainable Energy Fuels*, 2021, **5**, 2469–2476.

44 W. Zhao, Q. Tan, K. Han, D. He, P. Li, M. Qin and X. Qu, *J. Phys. Chem. C*, 2020, **124**, 12185–12194.

45 T. Liang, H. Wang, R. Wang, B. He, Y. Gong and C. Yan, *Electrochim. Acta*, 2021, **389**, 138686.

46 H. Wang, X. Wang, Q. Li, H. Li, J. Xu, X. Li, H. Zhao, Y. Tang, G. Zhao and H. Li, *ACS Appl. Mater. Interfaces*, 2018, **10**, 38862–38871.

47 J. Zhou, L. Ma, H. Song, B. Wu and X. Chen, *Electrochem. Commun.*, 2011, **13**, 1357–1360.

48 J. Wang, F. Kong, J. Chen, Z. Han, S. Tao, B. Qian and X. Jiang, *ChemElectroChem*, 2019, **6**, 2805–2811.

49 C. Masarapu, V. Subramanian, H. Zhu and B. Wei, *Adv. Funct. Mater.*, 2009, **19**, 1008–1014.